Journal of Materials Research and Technology 31 (2024) 718–732

Contents lists available at ScienceDirect

Journal of Materials Research and Technology

journal homepage: www.elsevier.com/locate/jmrt

Effect of the welding technique and post-welding heat treatments on the microstructure and mechanical properties of a high silicon nanostructured carbide-free bainitic steel

Mattia Franceschi [a,d,*], Edoardo Bregolin [b], Alvise Miotti-Bettanini [c], Luca Pasqualini [c], Simone Campagnolo [c], Andrea Zambon [a], Luca Pezzato [a], Manuele Dabalà [a]

[a] Department of Industrial Engineering, University of Padova, Via Marzolo 9, 35131, Padova, Italy
[b] Department of Industrial Engineering, University of Padova, Via Venezia 1, 35131, Padova, Italy
[c] INE SpA, Via Facca, 10, 35013, Cittadella, PD, Italy
[d] Department of Management and Engineering, University of Padova, Stradella San Nicola 3, 36100, Vicenza, Italy

ARTICLE INFO

Keywords:
Steel
Bainite
Welding
Mechanical properties

ABSTRACT

Recently carbide free bainitic steels, with microstructure consisting in nanoscaled bainitic ferrite plates and high carbon-enriched austenite, have been developed. These steels have found commercial use in manufacturing engineering components, nevertheless, their high carbon concentration poses a limitation as they cannot be welded, restricting their potential applications, therefore the actual research has shifted to the investigation to medium carbon steels. In this work, Butt weld – V groove weldment have been realized with a novel medium carbon high silicon carbide-free bainitic steel by means GMAW and GTAW. Optical microscopy, scanning and transmission electron microscopy and X-ray diffraction were used to characterize the microstructures of both the fusion and heat affected zone. Dilatometry was utilized to study the phase transformations during post-welding heat treatment. Tensile and micro-hardness tests were carried out to evaluate the mechanical properties in the as-weld state after post-welding heat treatment. The analysis shows the possibility to obtain high strength weldments with high integrity and high strength (>1 GPa) coupled with reasonable ductility and the absence of cold or hot cracking phenomena.

1. Introduction

In recent years a new generation of advanced high-strength steels with a nanostructured carbide-free bainitic (CFB) microstructure has emerged, establishing a promising candidate for several industrial applications, such as components for the railway industry, bearing, diesel injection systems, wind-drive generators [1]. Carbide-free bainitic steels are generally Si-based steels, characterized by a composite microstructure. It consists of bainitic ferrite and carbon-enriched austenite. A controlled design of chemical composition and the heat treatment allows to obtain ultrafine bainitic ferrite that enhances the material strength. On the other hand, austenite is stabilized at room temperature thanks to a significant concentration of Si (>1.5%) and/or Al. Due to the low solubility of both elements in cementite, its precipitation from the untransformed austenite is suppressed [2–4], and as a result, carbon remains in austenite, lowering the martensite start temperature (M_s) and enhancing the thermal stability at room temperature. Carbon enriched austenite contributes mainly to the material ductility, with the strain-induced transformations into martensite occurring under loading (TRIP effect) [5]. This results in exceptional combination of strength (>1.5 GPa), ductility (~20%), and toughness (close to 100 $MPam^{1/2}$) [6,7]. Carbon-enriched austenite could be present with a twofold morphology, e.g. films and blocks. The former are located between bainitic ferrite plates, and they are characterized by high carbon content and dislocation densities (~10^{15} m^{-2}) and, therefore, high mechanical and thermal stability. The latter are located between bainitic ferrite sheaves [8,9] and they are less stable compared to the films due to the lower carbon enrichment.

The mechanical properties enabled by nanostructured carbide-free bainite could open a new way of manufacturing structural parts with significantly reduced mass and increased durability. One fundamental fabrication process of manufacturing is welding, in which two or more

* Corresponding author. Department of Management and Engineering, University of Padova, Stradella San Nicola 3, 36100, Vicenza, Italy
E-mail address: mattia.franceschi@unipd.it (M. Franceschi).

https://doi.org/10.1016/j.jmrt.2024.06.075
Received 8 January 2024; Received in revised form 30 May 2024; Accepted 11 June 2024
Available online 14 June 2024
2238-7854/© 2024 The Authors. Published by Elsevier B.V. This is an open access article under the CC BY-NC-ND license (http://creativecommons.org/licenses/by-nc-nd/4.0/).

individual parts are joined together to form a metallurgical continuum resulting in a permanent joint. The weldability of carbon steels is conventionally assessed through their Carbon Equivalent (CE) [10], which in its simpler form can be written as $CE = C + Mn/6 + (Cr + Mo + V)/5 + (Ni + Cu)/15$, and good weldability is achieved for CE between 0.35 and 0.45. On the other hand, for high carbon bainitic steels CE could reach value well above 0.5, hence the weldability of bainitic steels is critical and needs to be evaluated carefully [11]. Initial research on the topic was conducted by Bhadeshia [4]. Then subsequent attempts were made using various welding methods [12], as Gas Tungsten Arc Welding (GTAW or TIG), with high carbon steels (0.55/0.82 wt%) [11], as reports Królicka in a recent comprehensive review [11]. Fang and co-authors proposed an innovative process, known as the Regeneration treatment [13–15], to avoid the degradation of the mechanical properties of the welded structures. This newly proposed technique involves transferring the as-welded joint into a furnace and holding it at a suitable temperature for a sufficient duration to transform the austenite, formed by the heat input of the welding process, into bainite, thereby preventing its transformation into brittle martensite during cooling to room temperature. This combination of welding procedure and heat treatment results in weldments not affected by cold cracks or martensite in the weld zone and the general degradation of the mechanical properties. Furthermore, by combining the regeneration treatment with the application of plastic deformation [15], the authors developed the rotary impacting trailed welding (RITW) method, which accelerates the bainitic transformation, as occurs in the ausforming treatments [16–20]. It is well known that the application of plastic deformation helps refining the final bainitic microstructure, promotes the nucleation of bainitic ferrite, accelerating the kinetics. In addition, the application of external stresses promotes variant selection, resulting in the formation of only few crystallographic variants of bainitic ferrite and, thus an isotropic transformation and a dramatic variation in the bainite morphology [16,19,21,22]. A few years later, Song and co-workers [13,23] proposed the two-pass welding method for the realization of bainitic weldments, where two welding guns travel consecutively to refine the prior austenite grain size in the fusion and the heat-affected zone, resulting in the acceleration of the bainitic microstructure.

Furthermore, Fang and co-authors [14] focused, in alternative to the arc-based welding, also on laser-based welding methods. The authors found that, compared to the conventional TIG, laser welding generates lower heat input, reducing the magnitude of tempering in the HAZ. As a result, the depletion of the mechanical properties is limited, and the strength of the joint is comparable to that of the base material. Other attempts were made adopting austenitic stainless steel as filler material, owing to the high tolerance to hydrogen embrittlement, however they resulted not adequate in terms of mechanical properties [24].

The previous research on weldability of high strength bainitic steels focused mainly on TIG and laser welding. Despite the effectiveness of such welding processes, their applicability to industrial parts remains low due to low deposition rate (for the TIG) and the limitation to very small thickness (for laser welding). Hence, further investigations on the weldability of bainitic steels are required. This work aims to provide a new composition to prepare high strength weldments with standard commercial consumables and high productivity processes such GMAW (Gas Metal Arc Welding) with a newly developed carbide-free bainitic steel with medium carbon (0.38 wt%) and high silicon contents (3.2 wt %), to promote the wide application of high strength steels.

2. Experimental procedure

2.1. Material

In this work, medium-carbon (0.38 wt%) high-silicon steel was used, with chemical composition reported in Table 1 [5,16,25–27] and starting martensitic microstructure deriving from the production process. A high silicon content (3.2 wt%) and aluminium (0.105%) were added as main alloying element to prevent cementite precipitation from austenite during the austempering treatment necessary to obtain a carbide-free bainitic microstructure. Finally, manganese was added for solution strengthening, increase hardenability and maintain a low martensite start temperature and obtain low-temperature bainite [28].

2.2. Experimental setup and methods

The weldments fabricated in this study consisted of two plates of the base metal with a length of 200 mm, a width of 100 mm, and a thickness of 10 mm, with an edge chamfering of 30° (Fig. 1). The weldments were obtained in flat position, and before welding, the plates were spot-welded to two carbon steel plates to ensure a constant geometry during the entire process; such additional plates were removed after the bead fabrication and cooling to room temperature. Preheating of the plates was performed with a gas flame at 200 °C (pre-heating

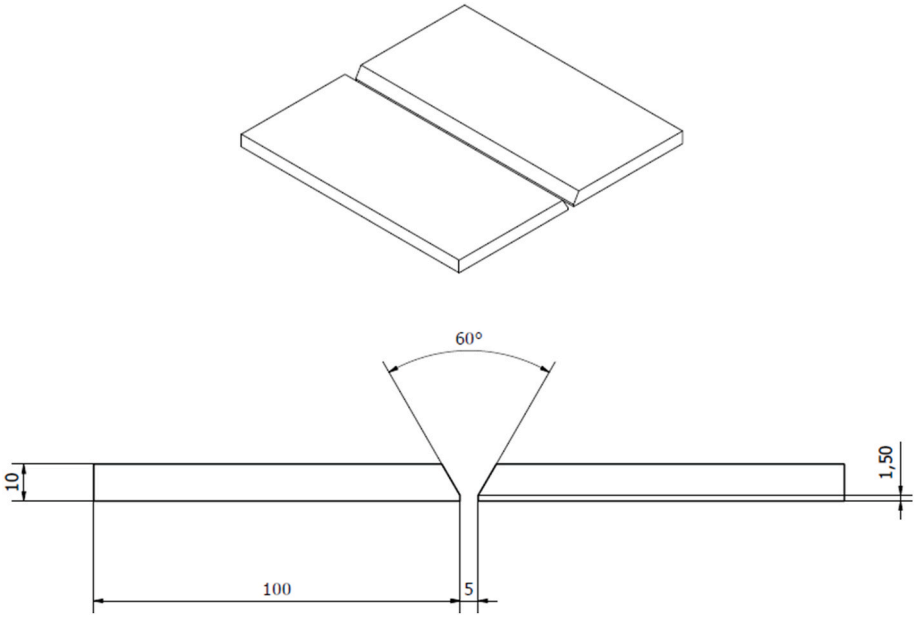

Fig. 1. Weld coupon scheme and edge details.

temperature). The temperature was selected based on preliminary experiment in order to avoid cracking and damage of the weldment due to the developed thermal stresses.

Two different welding techniques were adopted in this study: Gas metal arc welding (GMAW, UNI EN ISO 4063: 135) and GTAW (UNI EN ISO 4063: 141). All the weldments were realized with an INE SKYLINE KMD 5000 multi-process welding machine (INE SpA, Cittadella, Padova, Italy), equipped with an inverter-based generator, a separate wire feed system for continuous wire welding. GMAW welding was realized with 0.8 mm AWS A5.28 ER110S-G filler wire, with chemical composition shown in Table 2. The weldments were realized in Direct Current Electrode Positive (DCEP) mode, with the parameters reported in Table 3. GTAW coupon was realized with INETIG 120 S1 consumables (Table 2), with a 1.6 mm diameter and a WCe20 tungsten electrode was utilized on the torch side. The weld bead, completed in 14 passes, was realized in Direct Current Electrode Negative (DCEN) mode, with the welding conditions shown in Table 3.

2.3. Residual stress measurements

After welding, residual stress (RS) measurements were carried out by means X-ray diffraction method both along the longitudinal direction of the weld bead and the perpendicular direction. Five locations on the weldments were selected as illustrated in Fig. 2. A Spider X diffractometer (GNR Analytical Instrument Group S.r.l., Agrate Conturbia (NO), Italy) operating at 30 kV and 90 μA, with a chromium radiation tube and a vanadium filter for the Kβ positioned on the detector side, was used. The measurements were implemented using the (311) plane as the diffraction peak, and the ψ angle was varied, between −30 and 30°, considering in total of 11 angles. The diameter of the beam was set at 2 mm. Calculations of the stresses were carried out with the support of StressNet software, provided by the diffractometer supplier.

2.4. Penetrant dye liquid inspection

Penetrant dye liquid inspections were carried out on the upper surface of the weldments according to UNI EN 571-1 [29] and DIN EN ISO 16834. 2012 [30] standards, in order to reveal defects. The surface of each weldment was carefully cleaned with acetone to remove the impurities, then the penetrant liquid was sprayed on the surface of the weldment, and the excess liquid excess was removed by rinsing the surface with water. The deposited liquid remained on the surface of the weldment for 10 min and then the detector liquid was sprayed on the surface. Following the inspection, the weldments were cleaned with acetone.

2.5. Microstructural investigation

The weldments were sectioned transversally to the welding direction, at distance greater than 25 mm from the initial/final point of the bead, and specimens for microstructural investigation were extracted along the cross-section of the joint. The portions of material within the 25 mm from the bead's initial/final point were discarded to neglect the effect of the arc ignition and extinguishing according to the standard for the microstructural investigation of the welded joints. An entire transverse section was polished according to the standard metallographic procedure and etched with Klemm's I reagent, to reveal the macrostructure and then identify the fusion zone (FZ), the heat-affected zone (HAZ), the Base material (BM) and defects. Nital 2 etching solution was then adopted to reveal the microstructural constituents on the various zones of the weldments. After etching the microstructures were investigated by optical and scanning electron microscopy (Leica DMRE (Leica Microsystem S.r.l., Milan, Italy), Zeiss EVO MA10 (Carl Zeiss, Milan, Italy)). EBSD measurements were performed with a Tescan solaris (TESCAN, Brno, Czech Republic) operating at 20 kV, equipped with an Oxford EBSD (Oxford Instruments, Abingdon-on-Thames, UK) system and AzTec software. 100 × 100 μm^2 areas were scanned along the specimen's longitudinal direction. The procedure for EBSD measurements included etching-polishing cycles and final steps with 40 nm colloidal silica suspension.

XRD diffraction measurements for phase identification and quantification were performed with a Siemens D500 X-ray diffractometer (Siemens, Munich, Germany), a Cu tube monochromatic Kα radiation, working at 40 kV and 30 mA. 2θ = 40–105° angular range has been investigated with step scan of 0.025° and a counting time of 3s per step. For phase quantification, Rietveld analysis was performed with the support of Maud software [31]. Carbon content was determined according to the equation proposed by Cheng et al. [32].

TEM observations were performed with an FEI Tecnai G^2 TEM microscope operating at 100 kV. Sample preparation was performed according to the procedure described in Chapters 3 and 4, including mechanical thinning down to 50 μm with SiC papers, punching off 3 mm discs with a disc puncher and twin-jet electropolished, up to perforation, with a Struers Tenupol 3, and a 95% acetic acid (CH_3COOH) and 5% perchloric acid ($HClO_4$) solution used as the electrolyte, at 45 V, at room temperature.

2.6. Hardness measurements

Vickers microhardness profiles ($HV_{0.3}$) were obtained along the cross-section of the specimens, using a 300 g load and an indent spacing between two consecutive indentations at least three times the diagonal length.

2.7. Post-welding heat treatment and mechanical testing

Since the base material is designed to have a carbide free bainitic microstructure, austempering treatments were performed after the weldments fabrication. In addition, the microstructural evolution and the phase transformations of the welding consumables adopted in this study and in the HAZ were also evaluated.

Cylindrical samples for dilatometry from both the weld bead of GMAW and GTAW weldments and from the base material, with a 10 mm length and diameter of 4 mm, were machined utilizing wire electrodischarge machining along the weldment longitudinal direction. Dilatometric studies were performed during controlled thermal cycles with a BAHR DIL 805A/D (TA Instrument, New Castle, USA) high-resolution quenching dilatometer. Specimens were austenitized at 900 °C, at 10 °C/s heating rate (HR), in vacuum (5×10^{-4} mbar), then held for 5 min and rapidly cooled to room temperature (10 °C/s) to evaluate the critical temperatures (A_{c1}, A_{c3}, Ms), and detect possible transformations occurring upon cooling. Based on the estimated critical temperatures, shown below in the manuscript, and on previous studies showed elsewhere [5,33], the specimens were austenitized at 900 °C/s, after heating at 10 °C/s held for 5 min, cooled to 325 °C at 10 °C/s, and held for 3 h. Finally, the specimens were cooled to room temperature at 10 °C/s.

Specimens for uniaxial tensile tests were machined from the weldments along the transverse direction. Specimens with a thickness of 2 mm and width equal to the plate thickness and having the weld bead in the central part, were machined to have a uniform cross-section during tensile tests. An MTS 322 (MTS Systems Corporation, Eden Prairie, MN, USA) with a 50 kN load cell tensile test machine was adopted in this study. Before the tensile tests, each specimen was painted with a black-and-white spray to create a stochastic pattern of dots. For the entire duration of each tensile test, images of the tensile specimens were acquired with a high-speed camera and processed using the DIC software

Table 1
Chemical composition of the studied alloy (wt.%).

C	Si	Mn	Al	Cr	Ni	Mo	Cu	Fe
0.38	3.2	2.65	0.1	0.05	0.05	0.02	0.05	Balance

Table 2
Chemical composition of the wires and mechanical properties of the all weld metal deposit.

Consumable	AWS A5.28	Fe	C	Mn	Si	S	P	Cr	Ni	Mo	Cu	V	σ_Y (MPa)	σ_{UTS} (MPa)
INEFIL NiMoCr	ER110S-G	Bal.	0.08	1.60	0.50	0.007	0.007	0.30	1.50	0.25	0.12	0.09	790	820
INETIG 120 S1	ER120S-1	Bal.	0.08	1.90	0.80	0.007	0.007	0.40	2.15	0.25	0.15	0.10	800	900

Table 3
Welding parameters TS: Travel speed, HI: heat Input, IT: Interpass Temperature.

	GMAW	GTAW
Base material	High silicon Bainitic steel	High silicon Bainitic steel
Weldment geometry	Butt weld – V groove	Butt weld – V groove
Pre-heating	200 °C	200 °C
PWHT	Austempering	Austempering
Number od pases	6	14
Position	EN ISO 6947: PA	EN ISO 6947: PA
Consumable – EN/ AWS	EN ISO 16834-A: G 69 4 M21 Mn3Ni1CrMo AWS A5.28 ER110S-G	EN ISO 16834-A: W 79 6 I1 Mn4Ni2Mo AWS A5.28 ER120S-1
Consumable diameter	0.8 mm	1.6 mm
Shielding gas	EN ISO 14175: M21	EN ISO 14175: I1
Wire speed	11 m/min	–
Polarity	DCEP	DCEN
Current	168 A	188 A
Voltage	27 V	15 V
Travel Speed	37 cm/min	19 cm/min
HI	0.80 kJ/cm	0.91 kJ/cm
IT	200 °C	260 °C

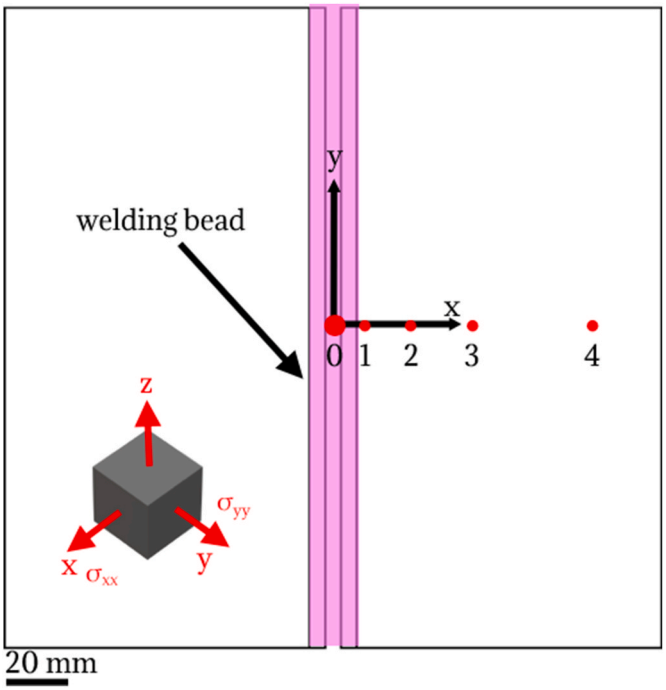

Fig. 2. Scheme of welded coupon illustrating the location of the RS measurements.

GOM Aramis™ to calculate the true strain in the gauge length.

3. Results and discussion

3.1. Penetrant dye liquids

The results of the dye penetrant inspection are shown in Fig. 3a and c. In all the cases macrocracks and defects were not detected on the surface. In case of the GMAW weldment a few red tracks on the surface were detected, corresponding to an accumulation of the liquid in correspondence with the slag flakes placed and metallic spatter on the surface of the bead (Fig. 3b). Indeed, during welding, the formed slag, forming as a consequence of the occurring chemical reactions, such as alloying element oxidation, that floats on the weld pool and solidifies on the surface, as displayed also in Fig. 3d. On the other hand (Fig. 3b), metallic spatters (red arrows) also form during the welding process near the arc and deposit and solidify in the vicinity of the weld bead.

3.2. As welded residual stresses

The residual stresses (RS) on the steel plates, in the "as-received" state, were first evaluated and it emerged that there was an average surface compressive residual stress state equal to −861 ± 35 MPa, ascribed to the manufacturing process of the studied material. Firstly, the slab after casting had been subjected to hot rolling and then underwent machining operations, performed to obtain a suitable surface finishing and the required geometry to perform the weldment (described in Fig. 1). It was established by Bertolini and co-authors [34] in a recent study, and the massive investigation carried out by Woo et al. [35–37], manufacturing procedures allow for the development of compressive stress that may affect the final residual stress state of components. Regarding the RS measurement and their distribution patterns in the GMAW and GTAW weldments (Fig. 4), it can be seen that the welding process induced tensile stresses on the coupons, contrasting the compressive initial state of the base material. In particular, in both the transverse and the longitudinal direction, in correspondence with the weld bead tensile residual stresses were found, in agreement with previous studies [38], and in all the cases were well below the yield strength of the material used to feed the chamfer. Then, the stress level progressively varies toward the compressive state increasing the distance from the bead. Moreover, it is noticeable that the level of residual stresses on the base material depends on the welding techniques, in agreement with Jiang and co-authors [38] and, in particular, GTAW weldment, which is characterized by an average larger heat input, induces larger residual stresses in the base material. The difference in the absolute values between GMAW and GTAW weldments is ascribed to the heat input related to the applied welding technique and the consequent heating rate. Madhavan et al. [39] determined that the higher the heat input the higher the magnitude of the final residual stresses in the weldment: considering the welding parameters adopted in this study, the number of passes and the lower welding speed related to each process, during GTAW the heat input was the largest compared to the other technique. Moreover, in the case of GMAW weldments, the used polarity connection was the DCEP, therefore most of the heat was provided to the electrode to melt and fill the joints, while in GTAW the working mode was the DCEN, and this results in a higher amount of heat received by the base metal and a larger heat affected zone. Furthermore, the difference in the stress levels between the longitudinal (Y) and the transverse (X) directions is induced by the heat flow occurring during welding, which is not homogeneous in the different directions, in agreement with Ouali et al. [40]. Heat is provided mainly along the welding direction, and this obviously reflects in the elongated shape of the isotherms in such direction. Due to the self-restraints deriving from the weld mock-up configuration, and assuming that no martensitic transformations take place in the solidified volume, upon cooling the build-up of tensile stresses along the longitudinal direction will clearly

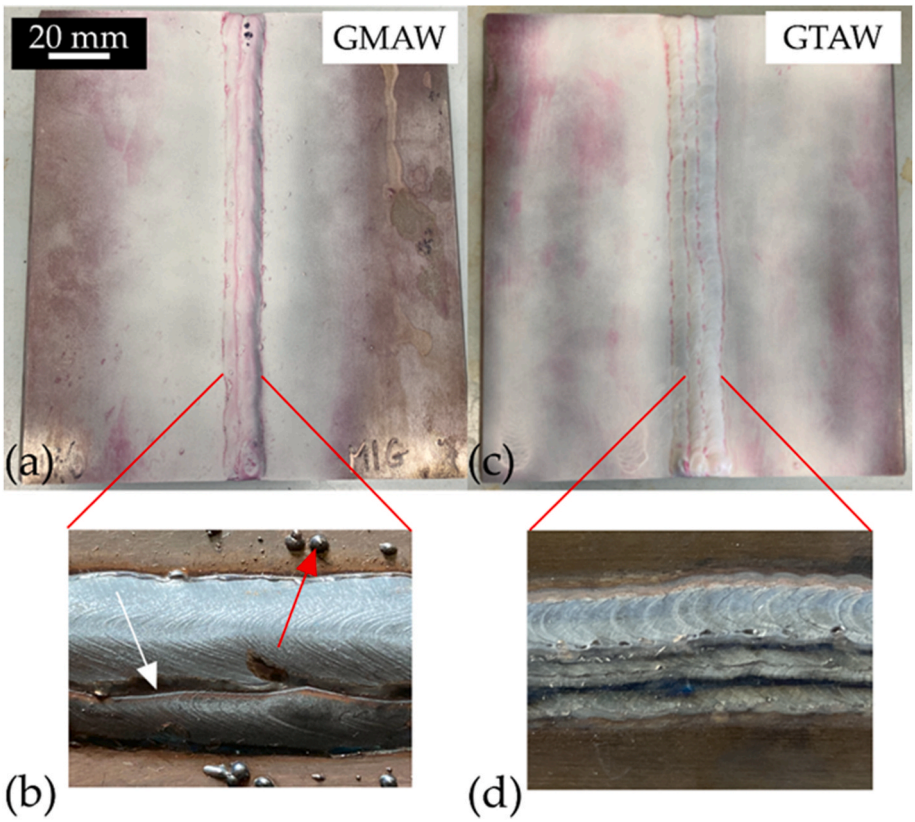

Fig. 3. Results of the penetrant dye liquids for the (a) GMAW, and (b) GTAW weldments and (b) Detail of the (c) GMAW and (d) detail bead surface (red arrow: metal sputter; white arrow: glassy slag).

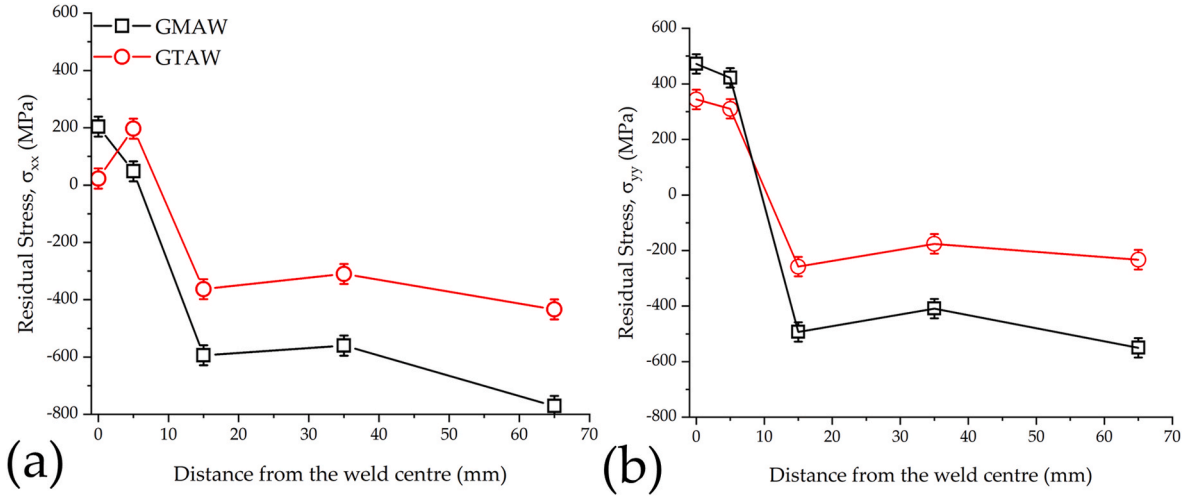

Fig. 4. Residual stress distributions in welded along the (a) transverse and (b) longitudinal direction for the GMAW and GTAW weldment.

surpass those developed in the transverse direction.

Finally, it was found that both welding process introduce continuous and symmetrical Z-direction distortions, equal to 1.1° ± 0.1° for the GMAW, and 2.3° ± 0.3° for the GTAW weldment, due to the thermally induced stresses (shrinkage stresses [41]). The greater distortions in the case of the GTAW weldment compared to the GMAW, coupled with the fracture in correspondence with the clamping system adopted to maintain the geometry, are correlated to larger heat input provided during the bead production. As speculated by Guo and co-authors [41], as the welding heat input increases, the transverse plastic strain also amplifies. This escalation causes a larger transverse shrinkage once the material cools. Consequently, this leads to an increase in transverse strain.

3.3. Microstructural characterization and hardness in as welded state

The overall view of weldments cross-section of the GMAW weldment is depicted in Fig. 5. It can be seen that both the weld cross-sections are characterized by heterogeneous structures which include a fusion zone (FZ) with a double V-bevel, the heat-affected zone (HAZ) and the base material. Optical microscope observations failed to detect macro defects such as hot/cold cracks, lack of penetration, lack of any inter-pass fusion, sidewall fusion and root fusion in the investigated cross section

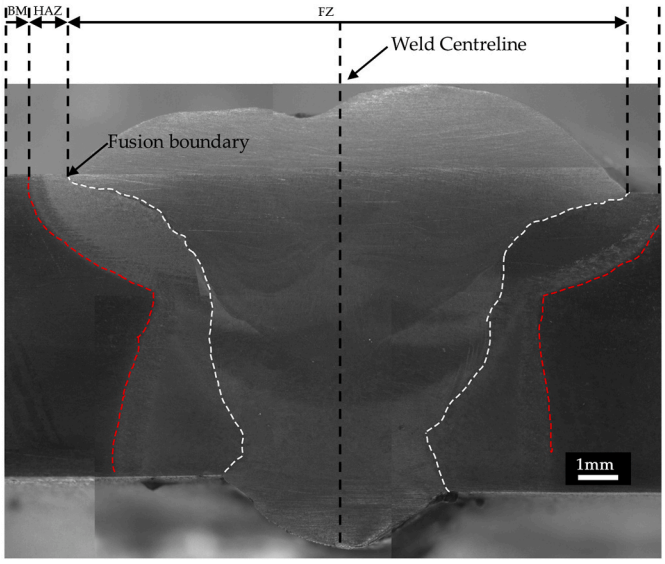

Fig. 5. Optical micrographs showing an overall view of the cross-section of the GMAW weldments.

[42]. The discrepancies in the chemical composition of the welded joints were also examined by means of SEM/EDS mapping analysis and elemental line profiles (Fig. 6) on the interface between heat-affected zone (HAZ) and weld metal (WM). HAZ is richer in Si and Mn, while WM is richer in Ni. Detailed micrographs of the FZ for the GMAW weldment are displayed in Fig. 7(a-c): the microstructure of the weld bead, with an average hardness of 280 $HV_{0.3}$ (Fig. 15a), mainly consists of an acicular ferrite matrix (α_C) with plates that exhibit a lenticular or lath shape, with a thickness of a few hundred nanometres, dispersed sulphide inclusions, as shows the EDS spectrum reported in Fig. 7d, and retained austenite is also present. As it can be observed in the TEM micrograph in Fig. 7 (b and c), the plates nucleate from the non-metallic inclusions dispersed within the weld bead [43]. SEM investigations and the acquired hardness profile (Fig. 15a) in the heat-affected zone led to distinguish three different sub-zones with different microstructural constituents, displayed in Fig. 8a-c, as a result of the thermal wave experienced during welding. Firstly, in the region next to the fusion boundary (Fig. 8a) the microstructure consists of untempered martensite since the heat provided by the process induces the complete austenitization of the material in such region. As a consequence, a peak in the hardness profile, with an average value of 645 $HV_{0.3}$ was detected as displayed in Fig. 15a. Moving along the cross section in the HAZ a second sub-region can be found, consisting of a mixture of bainitic ferrite and martensite/austenite, deriving from the full austenitization of the material and the continuous cooling of the weldments during the production. Finally, approaching the base material, a third sub-region consisting of tempered martensite with dispersed carbides, decorating the lath boundaries was also individuated. Corresponding to this, a "microhardness depression" is observed in the weldment cross-section, in which the local microhardness drops below 400 $HV_{0.3}$.

Similarly, for the GTAW weldment an overview of the weldment cross section is shown (Fig. 9), with the corresponding EDS mapping in Fig. 10. As observed in the formerly described junction, discrepancies in the chemical composition were detected. In particular, the heat affected zone appears richer in manganese and silicon, while the weld bead shows higher chromium content.

Focusing on the fusion zone, utilizing SEM and TEM (Fig. 11), it emerged that the bead microstructures consist again of acicular ferrite and retained austenite in the fusion zone, illustrated also through the EBSD IPF and the phase maps reported in Fig. 12 (a and b). It is worth mentioning that just a few particles of retained austenite were observed by means of EBSD due to the low resolution of the technique. Inclusion, oxides, and sulphides (Fig. 13), acting as nucleation sites for the acicular ferrite sub-units were also individuated in the fusion zone. From the EBSD IPF displayed in Fig. 12c it can be clearly seen that the acicular ferrite grows radially from the inclusions, with a gradual variation in the orientation in agreement with Milani et al. [44]. Finally, similarly to the GMAW weldments, microstructural constituents and three sub-regions were found in the HAZ, which is depicted in Fig. 14, suggesting that the same phase transformation occurred during the welding fabrication. However, despite the similar phase transformation products in the HAZ, a few differences emerged from analysing the hardness profile in Fig. 15. In particular, compared to the GMAW weldment, the first sub-region in the HAZ consisting of martensite appeared softer, with a hardness peak that does not exceed 500 $HV_{0.3}$. In principle, the differences should be traced back to the thermal cycle experienced by the material during the bead fabrication. Due to the higher number of passes required to fabricate the bead and the larger heat provided in the GTAW process, the

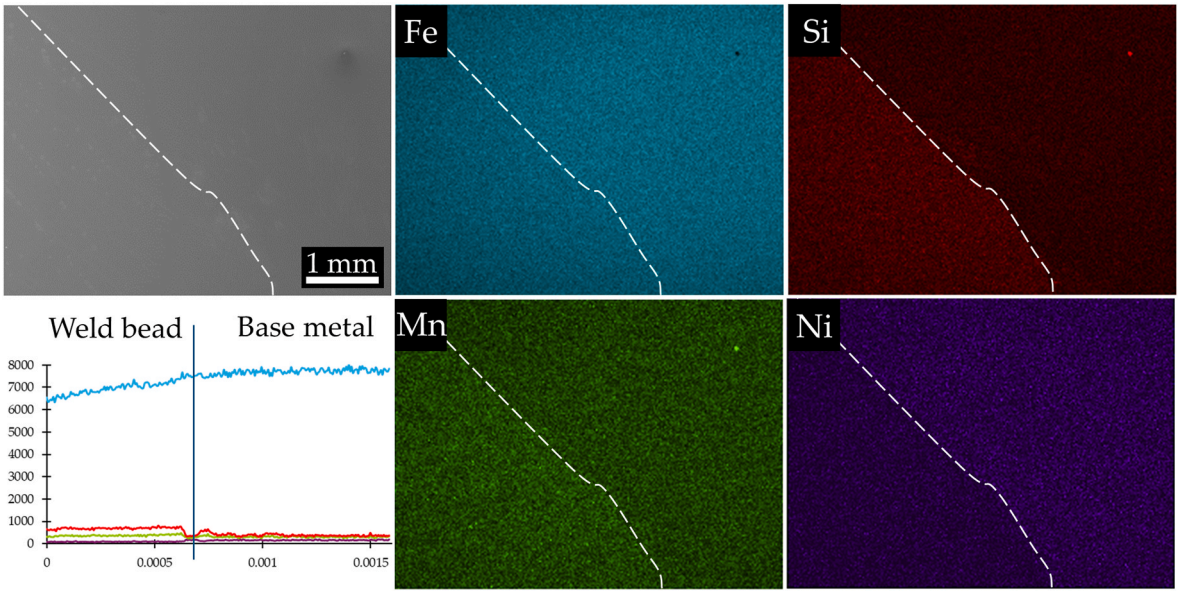

Fig. 6. EDS mapping and line analysis on the GMAW weldment.

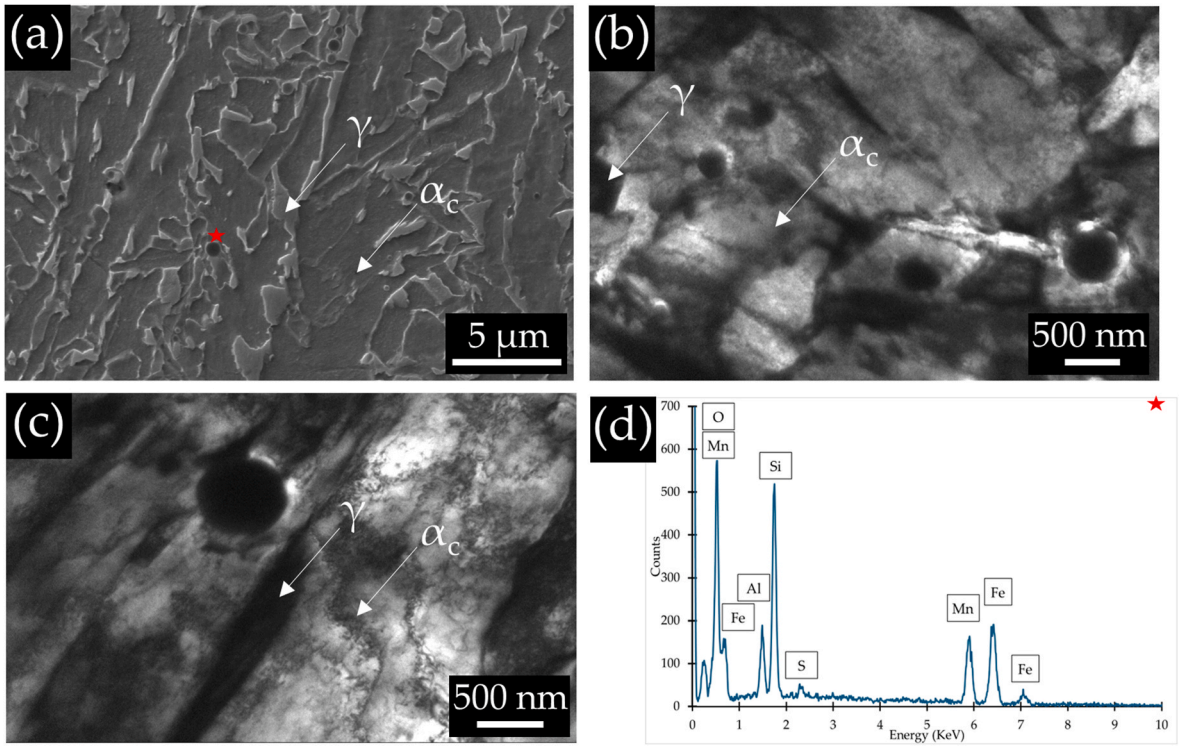

Fig. 7. (a) SEM, (b) and (c) TEM micrographs depicting the microstructure of the fusion zone of the GMAW weldment; the star in (a) indicates the location of the depicted EDS spectrum. α_C: acicular ferrite matrix, γ: austenite.

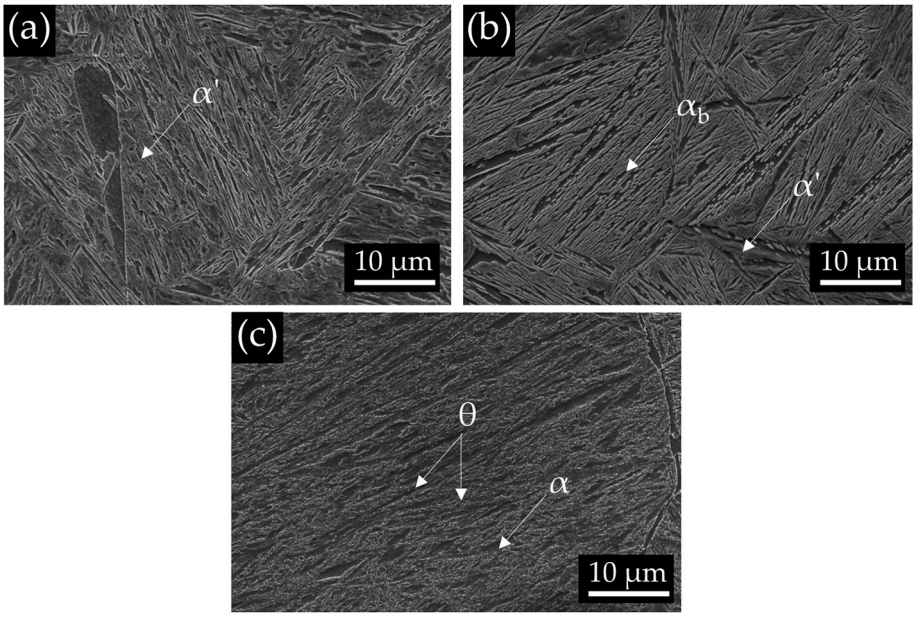

Fig. 8. (a), (b) and (b) SEM micrographs illustrating the microstructure of the heat affect zone in the GMAW weldment. α': acicular ferrite matrix, α_b: bainitic ferrite, θ:cementite.

portion of the material adjacent to the fusion boundary is subjected to a periodic re-heating, which may induce a more significative self-tempering effect of the microstructure. In martensitic microstructures, carbon atoms, just after the transformation, are distributed homogeneously in the octahedral sites of the bct lattice (Zener-Ordered) [45], however, during the reheating at low temperatures, the microstructure undergoes spinodal decomposition and there is the agglomeration of carbon atoms in clusters, with plate like-shape, at the sub-grain boundaries [45]. Cluster formation and the consequent reduction in the martensite carbon content tetragonality are responsible for the hardness reduction. Furthermore, from both the micrographs and the hardness measurements it emerges that GTAW welding produces wider HAZ compared to GMAW processing due to the combination of larger heat input and a larger number of passes to complete the weld bead.

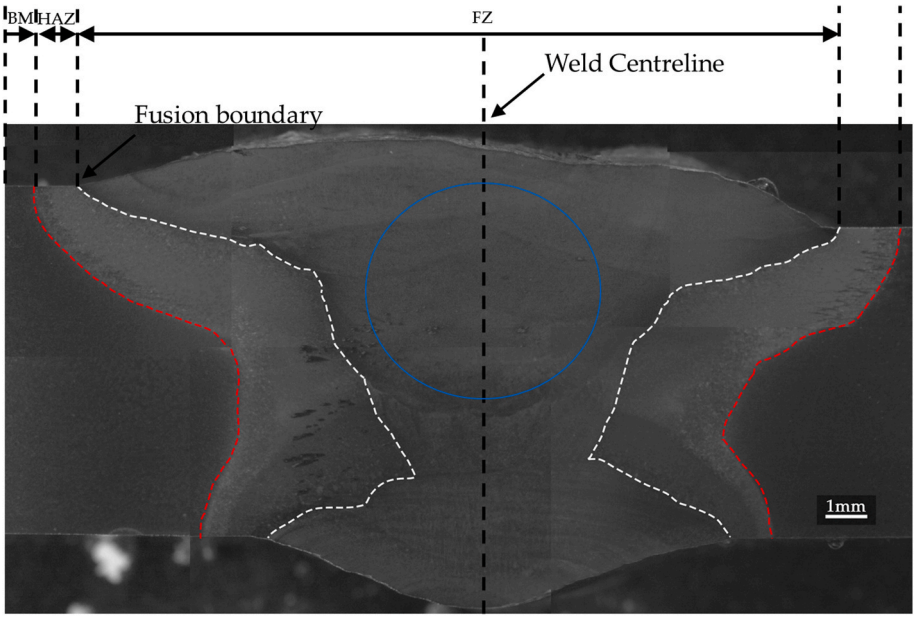

Fig. 9. Optical micrographs showing an overall view of the cross-section of the GTAW weldments. *the Blue circle indicates the dilatometric sample extraction zone.

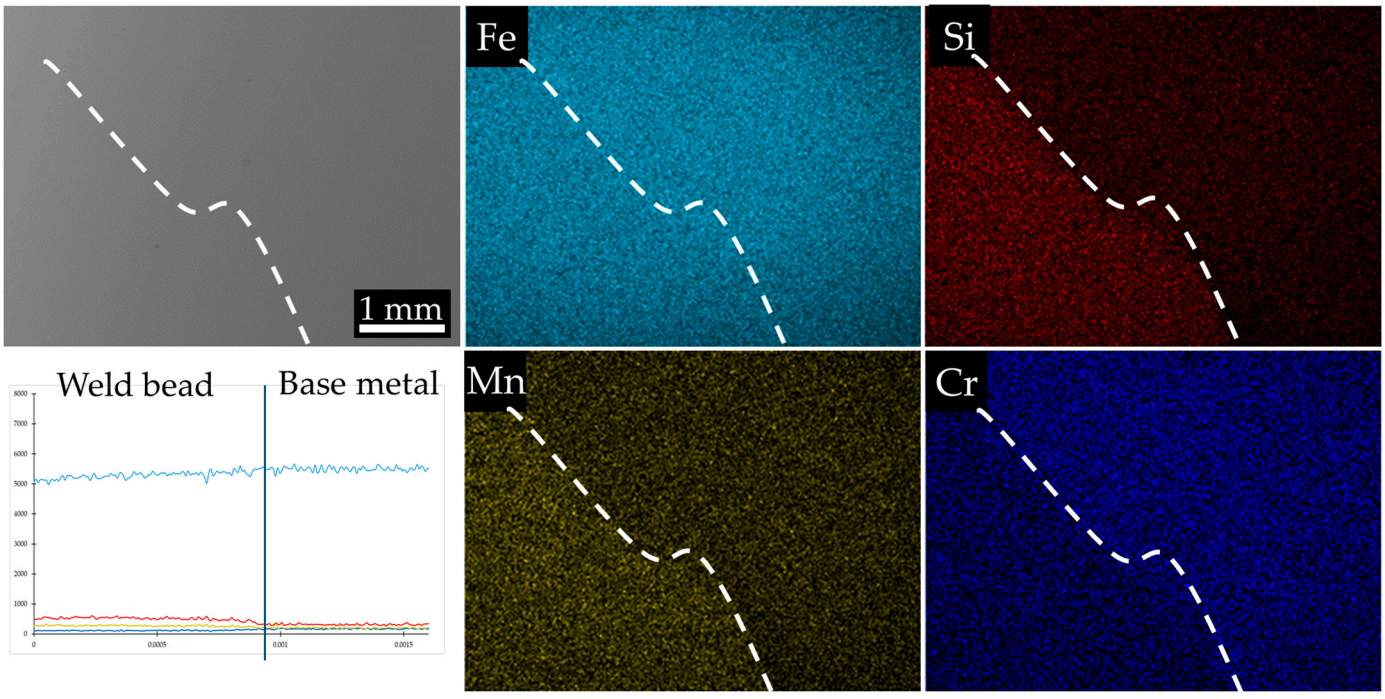

Fig. 10. EDS mapping and line analysis on the GTAW weldment.

3.4. Post-welding heat treatments

3.4.1. Dilatometric tests

In order to study the microstructural evolution of heat treatment and the reaction of the welding consumable to austempering treatment, dilatometric tests have been performed on the base material and the fusion zone produced with INEFIL NIMOCR and INETIG 120S1. Fig. 16a shows the typical dilatation curve obtained during the heat treatment cycle for the evaluation of the critical transformation temperatures, which are reported in Table 4. It is noticeable that the cooling stage for the GMAW welds, indicated by the arrow facing down, is characterized by linear contraction in the temperature range from 900 °C down to 521 °C. The absence of discontinuity in this temperature range confirms that the cooling rates were sufficiently high to avoid diffusive-type transformations, then a big hump is detected due to the formation of athermal martensite. Furthermore, a detailed analysis of the martensite formation shows a splitting phenomenon which is indicated by the red arrow in the corresponding Fig. 16. In particular, the non-isothermal austenite-to-martensite transformation does not occur continuously in a single step, as occurs for base material, due to possible segregations developed during welding, thus the transformation is split into different stages: the first starts at 521 °C, which corresponds to Ms1 and the second starts at 348 °C (Ms0), which indicates the start of the splitting described above [46]. Fig. 16b reports the cooling segment of the

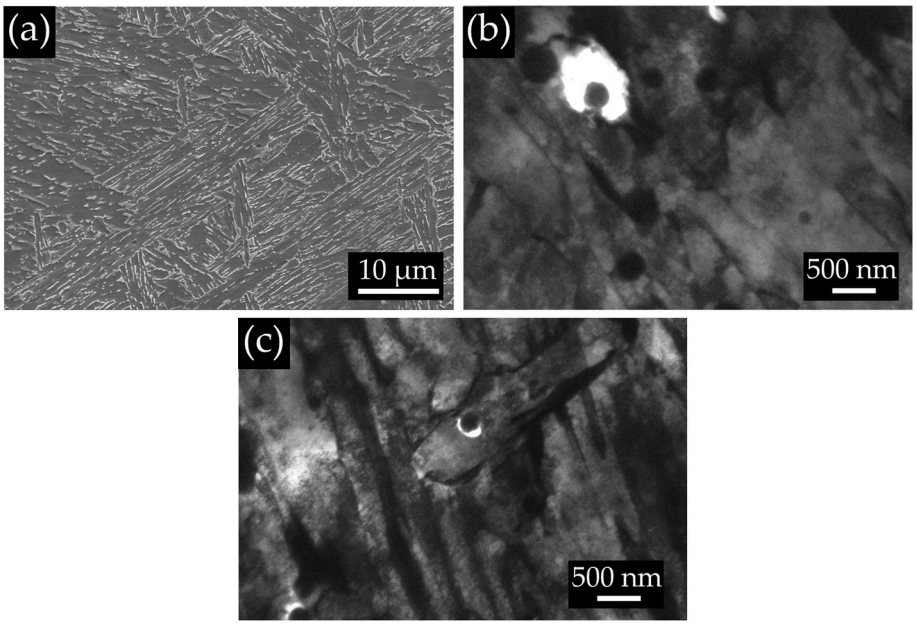

Fig. 11. (a) SEM and (b), (c) TEM micrographs depicting the microstructure of the fusion zone.

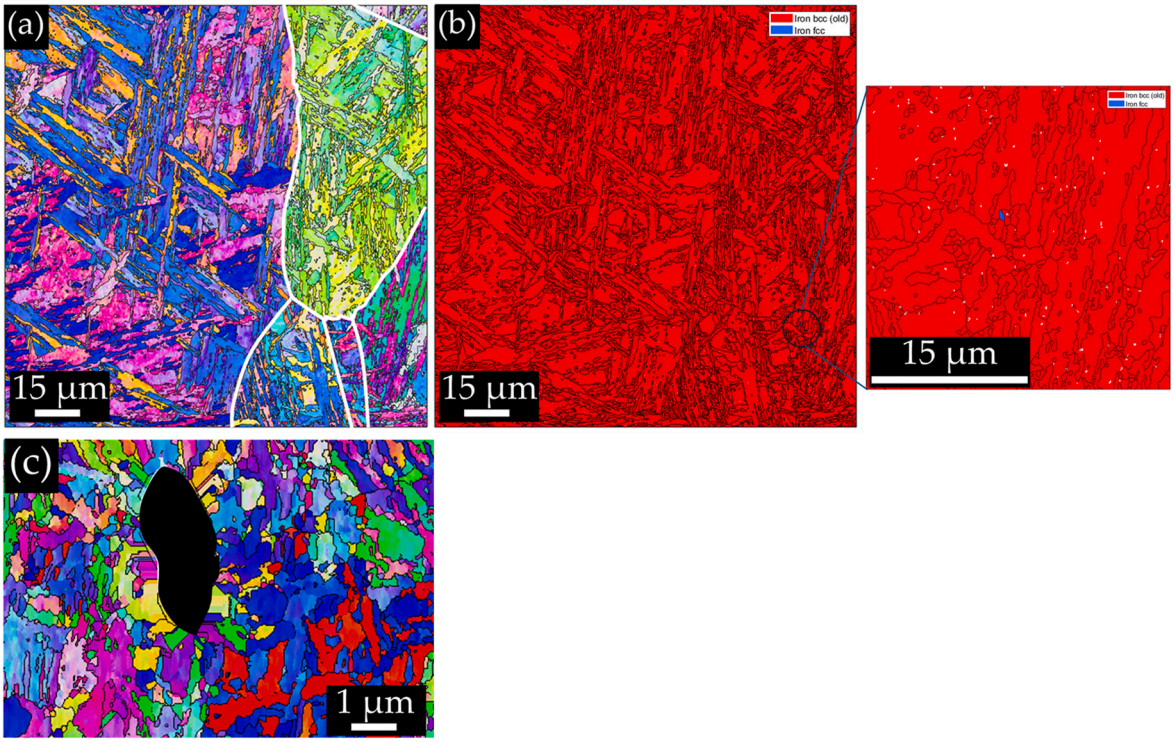

Fig. 12. EBSD (a) IPF and (b) Phase Distribution map acquired on the GTAW fusion zone.

Temperature vs relative change in length (RCL) curve recorded during the austempering treatment at 325 °C after austenitization at 900 °C. Concerning the base material, the specimen length increases following a sigmoidal path, which is reported, as a function of the holding time in Fig. 16c. Bainite growth is a displacive phenomenon, characterized by two strain contributions: a shear and a dilatation strain. According to Bhadeshia [47], the shear components are larger at least four times than the dilatation one, but considering that the bainitic reaction is isotropic, under the absence of external stresses, as in this part of the study, all the shear components cancel the final value, while the dilatation components sum up, thus any variation in length is associated to bainitic ferrite formation [19]. Furthermore, three different stages can be differentiated in the Time vs RCL (Fig. 16c): the curve is characterized by an incubation period, followed by a rapid positive dilatation, which indicates bainitic ferrite and a plateau corresponding to the completion of the bainitic transformation, reached after ~6250s, estimated according to Ref. [31].

On the other hand, in both GMAW and GTAW welds, the bainitic transformation follows the partial transformation of the undercooled austenite, into athermal martensite, in agreement with the estimated

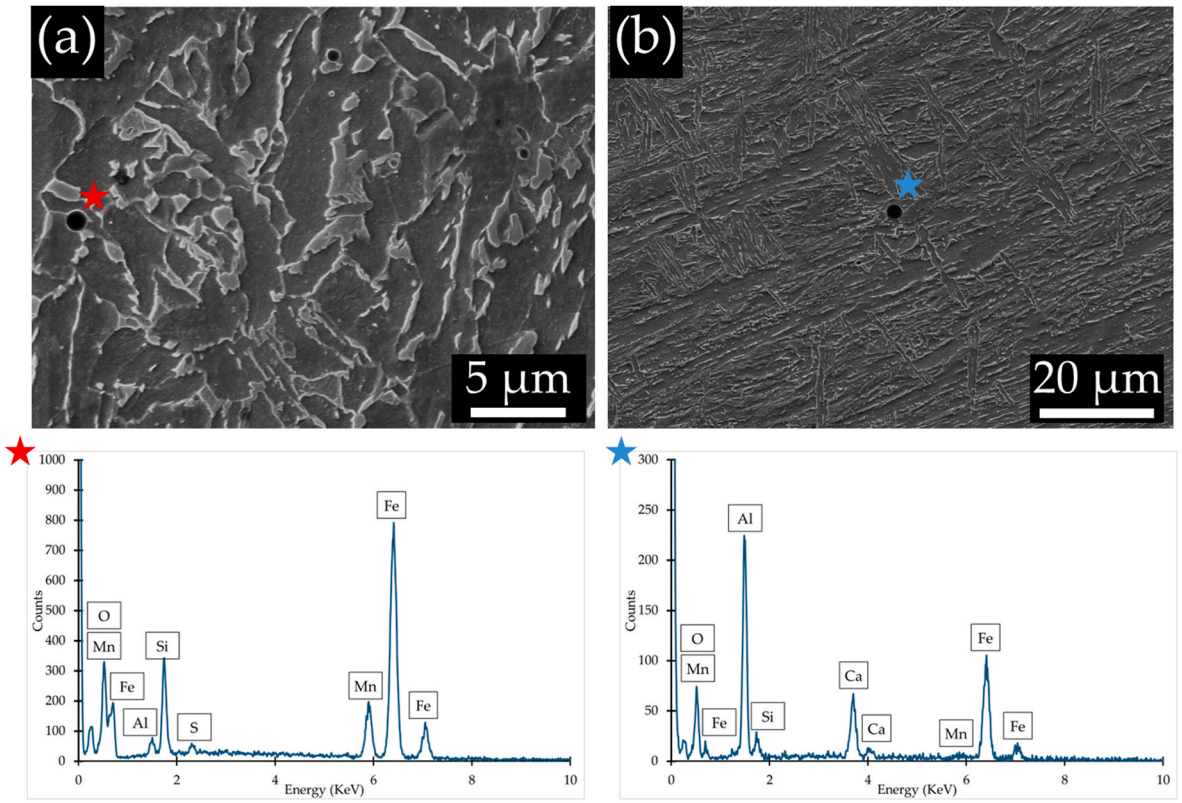

Fig. 13. EDS point analysis on the non-metallic inclusions observed in the weld bead. The coloured stars connect the inclusion and the collected EDS spectra.

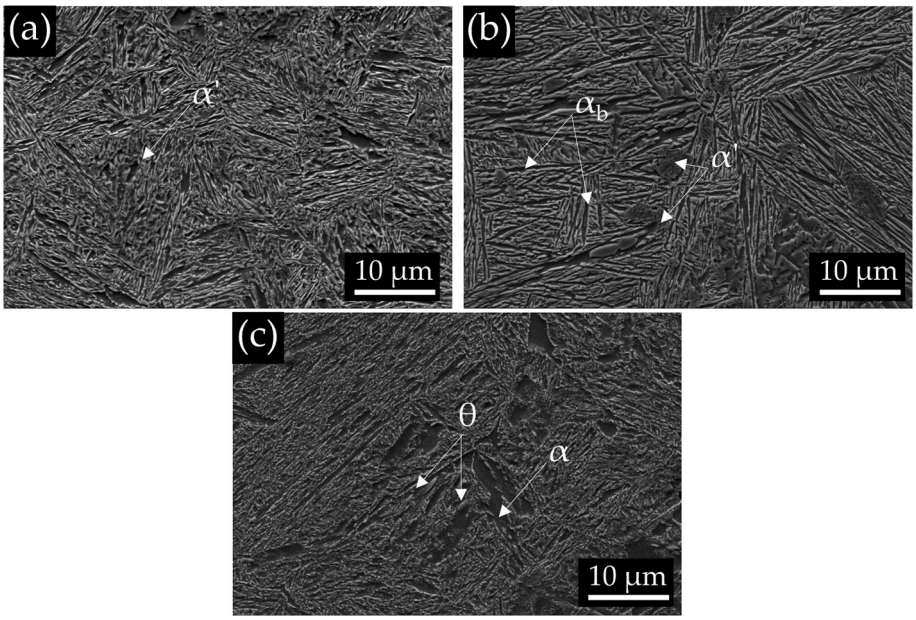

Fig. 14. (a), (b) and (b) SEM micrographs illustrating the microstructure of the heat affect zone in the GMAW weldment. α ': acicular ferrite matrix,α_b: bainitic ferrite, θ:cementite.

Ms, as shown in Fig. 16b. The expansion induced by the athermal martensite formation is then followed by a sudden positive dilatation, corresponding to the bainite formation, according to San Martin et al. [31]. During the isothermal stage, for both the adopted consumable, the variation of the specimen's length is not characterized by an incubation time suggesting that the further phase transformation is accelerated by the formation of martensite (Fig. 16c). According to Kawata and co-authors [49], the bainitic reaction is accelerated due to the introduction of new nucleation sites in correspondence with the newly developed austenite/martensite interfaces. Furthermore, this hypothesis of acceleration of the bainitic transformation, due to prior martensitic formation, finds support in the results of Toji and co-author [50], on the investigation of both Si-free and silicon-containing steel. In Si-free steels, as those adopted for the fabrication of the weld bead, bainite grows

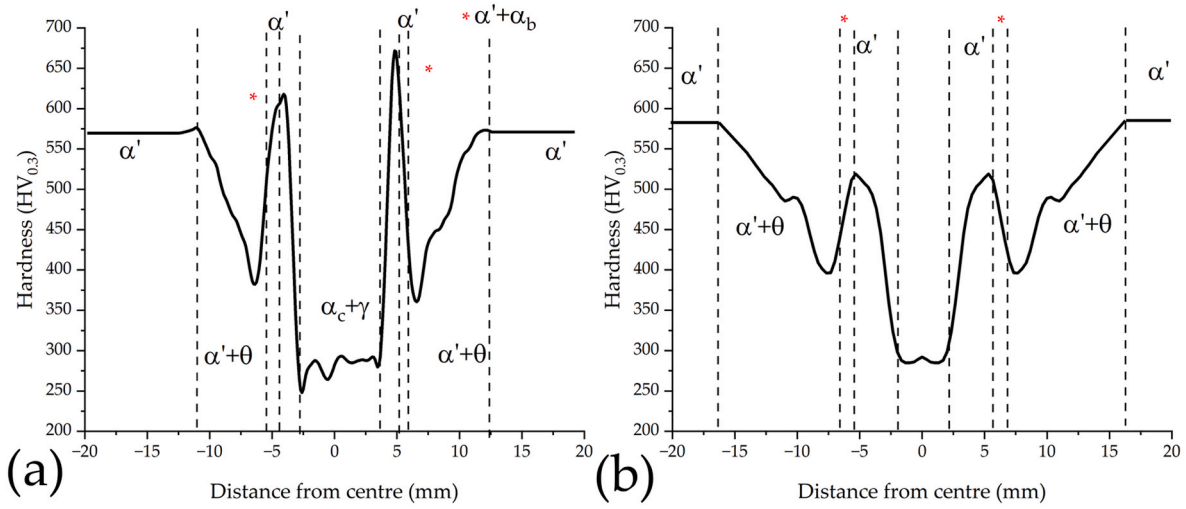

Fig. 15. Microhardness profile across the weldments cross-section (a) GMAW, (b) GTAW.

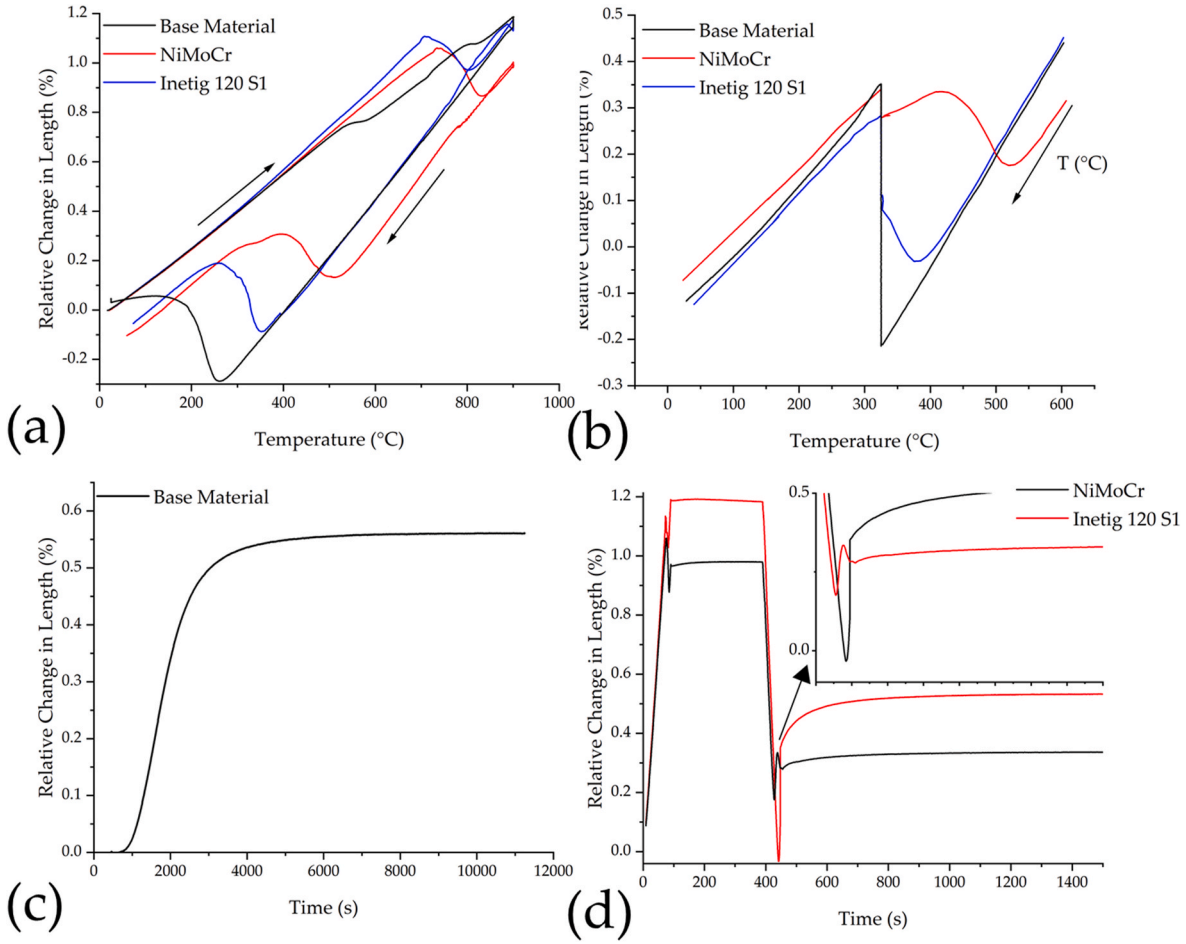

Fig. 16. Dilatometric curves recorded during post-welding heat treatment. (a) Temperature vs RCL curves for the estimation of the critical transformation temperature. (b) Cooling segment of the Temperature vs RCL curve recorded during the austempering treatment at 325 °C after austenitization at 900 °C; (c) Time vs RCL curve showing the bainitic ferrite formation in the base material during austempering at 325 °C; (d) (c) Time vs RCL curve showing the bainitic ferrite formation in the NiMoCr and Inetig 120 S1 steel during austempering at 325 °C.

surrounding the prior martensite [50]. Furthermore, the authors found that prior martensitic transformation controls the newly formed bainitic ferrite from a crystallographic point of view: irrespectively to the silicon content, in their case, the orientation relationship between austenite and bainitic ferrite changes from a Nishiyama-Wassermann (N–W) to Greninger-Troiano (G-T) OR.

3.4.2. *Microstructural and mechanical investigation*

After austempering treatment at 325 °C the base material, irrespective to the welding technique, is characterized by the typical

Table 4
Critical transformation temperature estimated from the dilatometric curves adopting the 0.02 % offset method [48].

Material	Ac1 (°C)	Ac3 (°C)	Ms (°C)
Base Material	790	834	268
GMAW fusion zone	735	861	521
GTAW fusion zone	720	837	356

carbide-free bainitic microstructure consisting of bainitic ferrite plates and carbon-enriched austenite with a double morphology, untransformed blocks between the sheaves and film sandwiched between the ferrite sub-units (Fig. 17), in agreement with previous studies by the same authors [33]. The average bainitic ferrite plate thickness was estimated equal to 83 ± 39 nm, utilizing the linear intercept method, with utilizing at least five SEM micrographs and 40 measurements in each, for a minimum of 200 measurements for statistical significance. Furthermore a stereological correction have been applied according to Ref. [51].

Concerning the fusion zone of both weldments, in the central part of the bead for both the GMAW and the GTAW weldments, the microstructure consists of a mixture of martensite, bainite, and retained austenite as depicted in Fig. 17b and c. Fig. 17c and e displays the microstructure at the interface between the base material and the fusion zone. Irrespectively to the adopted technique, a portion of the base material, which is wider in the case of the GTAW weldments, is not characterized by the conventional expected bainitic microstructure, but bainitic sheaves are sandwiched by large ferritic islands and coalesced bainite, with the span in the order of several microns. The hardness profiles (Fig. 18), in addition, revealed that both on the base material and in the fusion the hardness is constant regardless of the processes.

The following section shows the mechanical performances of the two weldments after the post-welding heat treatments. The standard tensile properties 0.2% yield strength (YS), and ultimate tensile strength (UTS), estimated from the tensile test curves are reported in Table 5. From the tensile properties shown in Table 5, it emerged that both weldments are characterized by high tensile strength paired with a reasonable ductility, confirmed by the morphology of the fracture surface, with the typical

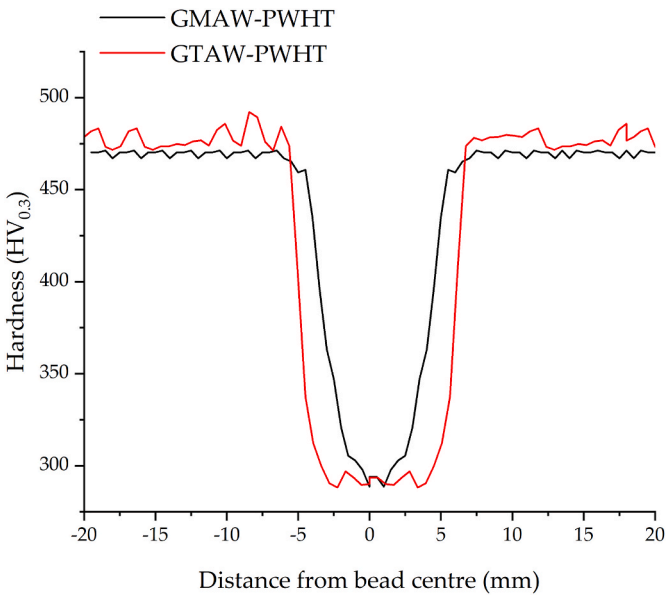

Fig. 18. Hardness profiles, after austenitization at 900 °C for 5 min and isothermal treatment at 325 °C for 3 h.

Table 5
Tensile test data of the investigated weldments.

Weld coupon	$\sigma_{Y0.2}$ (MPa)	σ_{UTS} (MPa)	RA (%)
GMAW	636 ± 2	1016 ± 2	38 ± 2
GTAW	803 ± 3	1292 ± 10	47 ± 5

cup-cone fracture and the dimples highlighted by the magnified micrograph Fig. 19. Moreover, both yield and ultimate tensile strength of the GMAW are reduced compared to the GTAW welding, while the elongation to failure is improved. The better performances are mainly attributed to better properties of the welding consumables adopted for

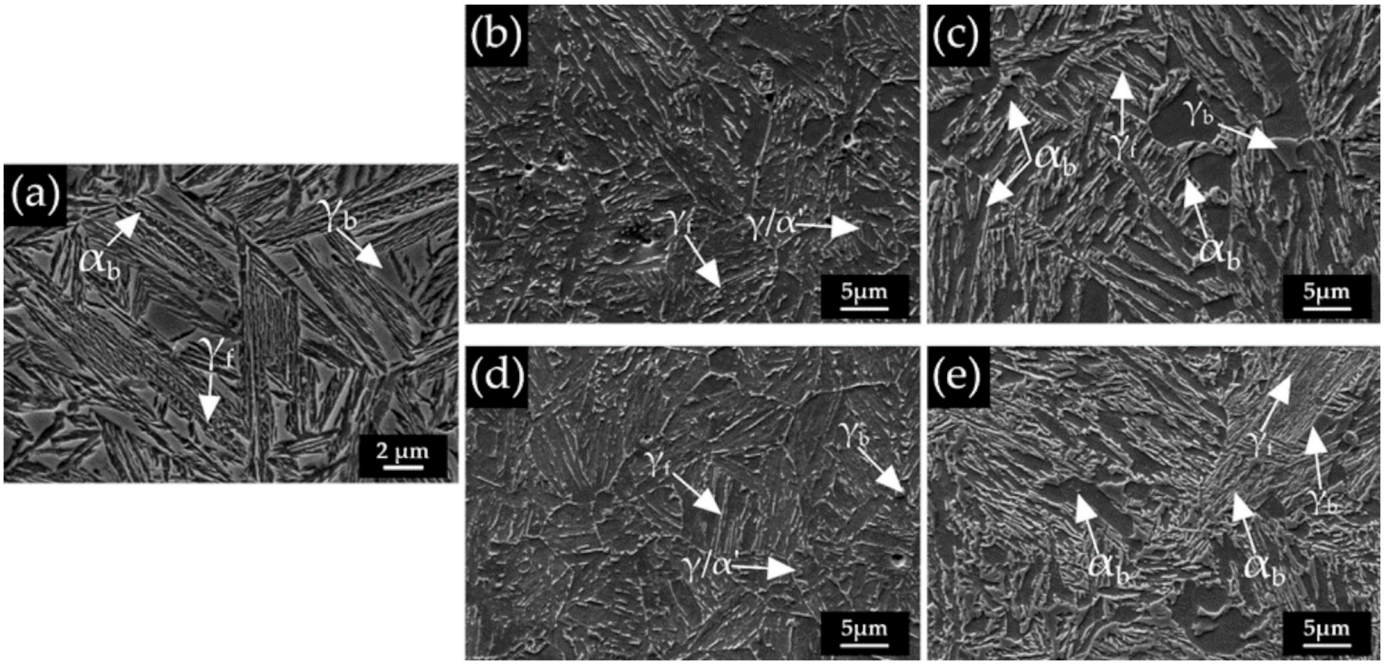

Fig. 17. SEM micrograph of (a) base material, (b) GMAW fusion zone, (c) GMAW dilution zone, (d) GTAW fusion zone, (e) GMAW dilution zone, after austenitization at 900 °C for 5 min and isothermal treatment at 325 °C for 3 h.

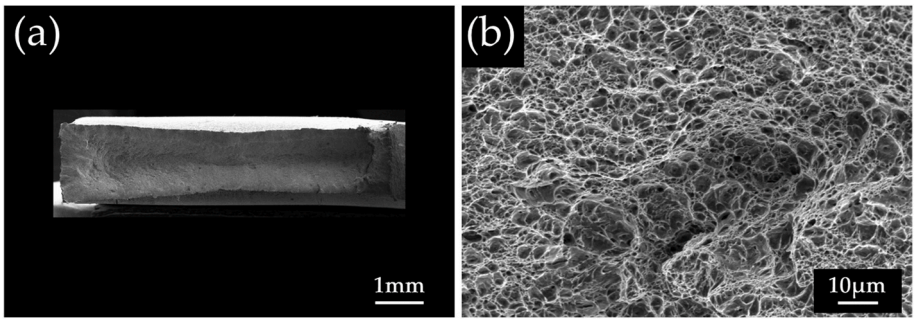

Fig. 19. Fracture surface from the GMAW weldment.

the GTAW weldment.

The strain maps before fracture are represented in Fig. 20. Pairing the tensile data with the localized strain image acquired with the ARAMIS system indicates that the strain distribution is clearly inhomogeneous within the tensile specimens.

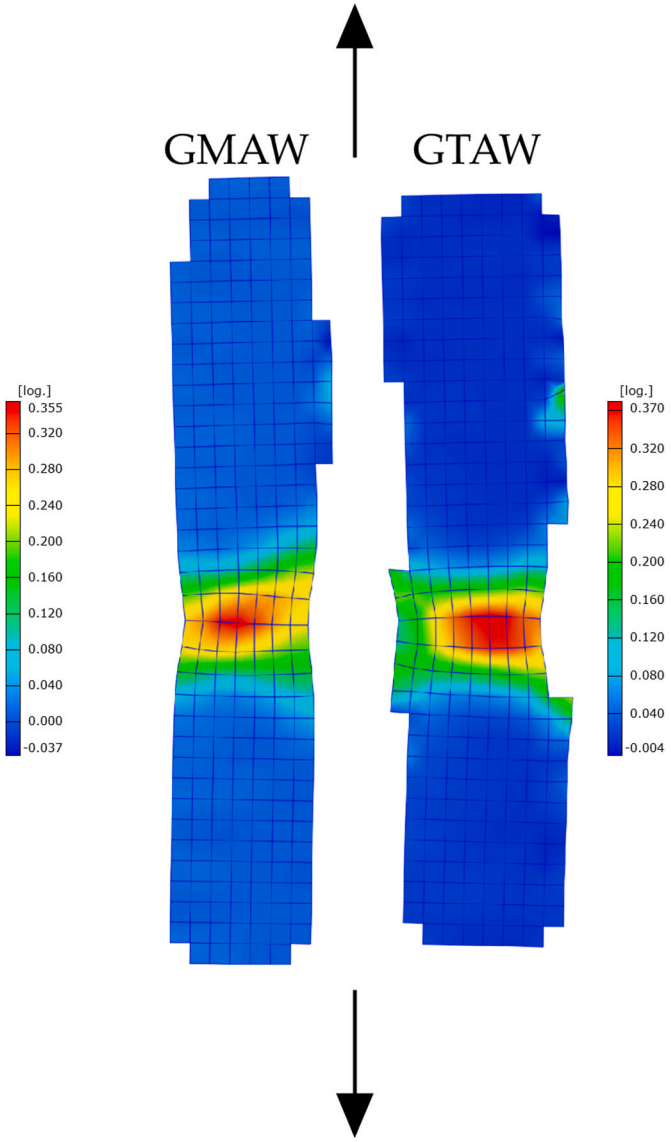

Fig. 20. Strain distributions obtained by DIC approach for the GMAW and GTAW weldment after PWHT.

4. Conclusions

The new composition of carbide free bainitic steel was successfully welded with GMAW and GTAW techniques using commercially available consumables. Welds produced are not sensitive to hot or cold cracking phenomena.

- Regardless of the technique used, welding induces residual tensile stresses in the weld zone and in the heat-affected zone longitudinally (parallel to the weld bead). However, these stresses are below the yield strength of the consumables used. Additionally, the thermal input from welding induces relaxation of stresses present in the base material.
- The heat-affected zone comprises different sub-regions with varying microstructures: particularly martensite, martensite plus bainite/retained austenite, and tempered martensite with cementite precipitates.
- The heat treatment highlights the presence of a decarburized zone at the boundary between the molten zone and the heat-affected zone induced by the welding process.
- During the austempering treatment on the weld bead, considering the low carbon content of the consumables, formation of martensite before bainitic transformation was observed.
- From the tensile tests it emerged the possibility to achieve welds with high mechanical strength, with ultimate tensile strength exceeding 1 GPa and reasonable ductility. Moreover, during mechanical tests, it was observed though DIC, that deformation is mainly concentrated in the weld bead, and fracture occurs within the weld bead.
- Despite the high mechanical strength of the welded joints, it is worth mentioning that the obtained values are well below those corresponding to the base material. Therefore, there is a need to develop consumables capable of ensuring similar performance with compositions and microstructures analogous to those of the base material or other third-generation AHSS steels.

Funding

Project supported by the BIRD 2021 program of the University of Padova and by the Interconnected Nord-Est Innovation Ecosystem (iNEST) funded by the Italian Government in the frame of the PNRR action.

Data availability

Data will be made available on request.

CRediT authorship contribution statement

Mattia Franceschi: Formal analysis, Investigation, Data curation, Writing – original draft, Writing – review & editing. **Edoardo Bregolin:** Formal analysis. **Alvise Miotti-Bettanini:** Methodology, Writing –

original draft, Writing – review & editing. **Luca Pasqualini:** Methodology. **Simone Campagnolo:** Formal analysis. **Andrea Zambon:** Methodology, Writing – review & editing, Supervision. **Luca Pezzato:** Project administration, Funding acquisition, Visualization, Writing – original draft, Writing – review & editing. **Manuele Dabalà:** Project administration, Funding acquisition, Visualization.

Declaration of competing interest

The authors declare that they have no known competing financial interests or personal relationships that could have appeared to influence the work reported in this paper.

Acknowledgements

The authors gratefully acknowledge the support provided by dilatometry laboratory belonging to UCLOUVAIN; Mattia Franceschi would like to express his gratitude to prof. Pascal Jacques for providing access to the laboratory facilities.

References

[1] Morales-Rivas L. Viewpoints on Technological aspects of advanced high-strength bainitic steels. Metals 2022;12. https://doi.org/10.3390/met12020195.
[2] Garcia-Mateo C, Caballero FG, Sourmail T, Kuntz M, Cornide J, Smanio V, Elvira R. Tensile behaviour of a nanocrystalline bainitic steel containing 3wt% silicon. Mater. Sci. Eng. A 2012;549:185–92. https://doi.org/10.1016/j.msea.2012.04.031.
[3] Qian L, Zhou Q, Zhang F, Meng J, Zhang M, Tian Y. Microstructure and mechanical properties of a low carbon carbide-free bainitic steel Co-alloyed with Al and Si. Mater Des 2012;39:264–8. https://doi.org/10.1016/j.matdes.2012.02.053.
[4] Bhadeshia HKDH, Load M, Svensson L. Silicon-rich bainitic steel welds. Trans JWRI 2003:43–52.
[5] Franceschi M, Miotti Bettanini A, Pezzato L, Dabalà M, Jacques PJ. Effect of multi-step austempering treatment on the microstructure and mechanical properties of a high silicon. Metals 2021;11:17. https://doi.org/10.3390/met11122055.
[6] Garcia-Mateo C, Caballero FG. Understanding the mechanical properties of nanostructured bainite. Handb. Mech. Nanostructuring 2015;1:35–65. https://doi.org/10.1002/9783527674947.ch3.
[7] Garcia-Mateo C, Sourmail T, Caballero FG, Smanio V, Kuntz M, Ziegler C, Leiro A, Vuorinen E, Elvira R, Teeri T. Nanostructured steel industrialisation: plausible reality. Mater Sci Technol 2014;30:1071–8. https://doi.org/10.1179/1743284713Y.0000000428.
[8] Mousalou H, Yazdani S, Avishan B, Ahmadi NP, Chabok A, Pei Y. Microstructural and mechanical properties of low-carbon ultra-fine bainitic steel produced by multi-step austempering process. Mater. Sci. Eng. A 2018;734:329–37. https://doi.org/10.1016/j.msea.2018.08.008.
[9] Singh K, Kumar A, Singh A. Effect of prior austenite grain size on the morphology of nano-bainitic steels. Metall. Mater. Trans. A Phys. Metall. Mater. Sci. 2018;49:1348–54. https://doi.org/10.1007/s11661-018-4492-8.
[10] Goto S, Kami C, Kawamura S. Effect of alloying elements and hot-rolling conditions on microstructure of bainitic-ferrite/martensite dual phase steel with high toughness. Mater. Sci. Eng. A 2015;648:436–42. https://doi.org/10.1016/j.msea.2015.09.093.
[11] Królicka A, Ambroziak A, Zak A. Welding capabilities of nanostructured carbide-free bainite: review of welding methods, materials, problems, and perspectives. Appl Sci 2019;9:1–15. https://doi.org/10.3390/app9183798.
[12] Kirbiš P, Vuherer T, Irgolič T, Anžel I. Metallographic analysis of kinetically activated bainite (KAB) welds. Metallogr. Microstruct. Anal. 2015;4:570–8. https://doi.org/10.1007/s13632-015-0234-0.
[13] Fang K, Yang JG, Liu XS, Song KJ, Fang HY, Bhadeshia HKDH. Regeneration technique for welding nanostructured bainite. Mater Des 2013;50:38–43. https://doi.org/10.1016/j.matdes.2013.02.019.
[14] Fang K, Yang JG, Song KJ, Liu XS, Wang JJ, Fang HY. Study on tempered zone in nanostructured bainitic steel welded joints with regeneration. Sci Technol Weld Join 2014;19:572–7. https://doi.org/10.1179/1362171814Y.0000000227.
[15] Fang K, Yang JG, Song KJ, Liu XS, Fang HY. Acceleration of regeneration treatment for nanostructured bainitic steel by rotary impacting trailed welding. J Mater Process Technol 2014;214:2935–40. https://doi.org/10.1016/j.jmatprotec.2014.06.024.
[16] Franceschi M, Bertolini R, Fabrizi A, Dabalà M, Pezzato L. Effect of ausforming temperature on bainite morphology in a 3.2% Si carbide-free bainitic steel. Mater. Sci. Eng. A 2023. https://doi.org/10.1016/j.chemosphere.2022.135907.
[17] Eres-Castellanos A, Morales-Rivas L, Jimenez JA, Caballero FG, Garcia-Mateo C. Effect of ausforming on the macro- and micro-texture of bainitic microstructures. Metall. Mater. Trans. A Phys. Metall. Mater. Sci. 2021;52:4033–52. https://doi.org/10.1007/s11661-021-06363-w.
[18] Garcia-Mateo C, Eres-Castellanos A, Somani M, Porter D, Latz A, Lieven B, Caballero FG. Developing nanostructured bainite by means of ausforming. In: Proceedings of the THERMEC 2018; 2018.
[19] Eres-Castellanos A, Morales-Rivas L, Latz A, Caballero FG, Garcia-Mateo C. Effect of ausforming on the anisotropy of low temperature bainitic transformation. Mater Char 2018;145:371–80. https://doi.org/10.1016/j.matchar.2018.08.062.
[20] He B, Xu W, Huang M. Effect of boron on bainitic transformation kinetics after ausforming in low carbon steels. J Mater Sci Technol 2017;33:1494–503. https://doi.org/10.1016/j.jmst.2017.05.006.
[21] Eres-Castellanos A, Hidalgo J, Morales-Rivas L, Caballero FG, Garcia-Mateo C. The role of plastic strains on variant selection in ausformed bainitic microstructures studied by finite elements and crystal plasticity simulations. J Mater Res Technol 2021;13:1416–30. https://doi.org/10.1016/j.jmrt.2021.05.070.
[22] Eres-Castellanos A, Zorgani M, Shahriari D, Romanica R, Jimenez JA, Garcia-Mateo C, Jahazi M. Effect of the ausforming deformation mode on bainitic transformation in a medium carbon high silicon steel. J Mater Res Technol 2022;18:3428–42. https://doi.org/10.1016/j.jmrt.2022.04.033.
[23] Song W, Liu X, Berto F, Razavi SMJ. Low-cycle fatigue behavior of 10CrNi3MoV high strength steel and its undermatched welds. Materials 2018;11. https://doi.org/10.3390/ma11050661.
[24] Krishna Murthy N, Janaki Ram GD, Murty BS, Reddy GM, Rao TJP. Carbide-free bainitic weld metal: a new concept in welding of armor steels. Metall Mater Trans B Process Metall Mater Process Sci 2014;45:2327–37. https://doi.org/10.1007/s11663-014-0120-1.
[25] Franceschi M, Pezzato L, Gennari C, Fabrizi A, Polyakova M, Konstantinov D, Brunelli K, Dabalà M, Dabal M. Effect of intercritical annealing and austempering on the microstructure and mechanical properties of a high silicon manganese steel. Metals 2020;10:1–19. https://doi.org/10.3390/met10111448.
[26] Franceschi M, Pezzato L, Settimi AGAG, Gennari C, Pigato M, Polyakova M, Konstantinov D, Brunelli K, Dabalà M, Dabal M. Effect of different austempering heat treatments on corrosion properties of high silicon steel. Materials 2021;14:1–17. https://doi.org/10.3390/ma14020288.
[27] Franceschi M, Soffritti C, Fortini A, Pezzato L, Garagnani GL, Dabalà M. Evaluation of wear resistance of a novel carbide- free bainitic steel. Tribol Int 2023;178. https://doi.org/10.1016/j.triboint.2022.108071.
[28] Garcia-Mateo C, Caballero FG, Bhadeshia HKDH. Low temperature bainite. J. Phys. IV Fr 2003;112:255–88. https://doi.org/10.1051/jp4.
[29] Penetrant testing UNI EN 571-1.
[30] Iso EN. Din en Iso 16834. 2012.
[31] San-Martin D, Kuntz M, Caballero FG, Garcia-Mateo C. A new systematic approach based on dilatometric analysis to track bainite transformation kinetics and the influence of the prior austenite grain size. Metals 2021;11:1–13. https://doi.org/10.3390/met11020324.
[32] Cheng L, Bottger A, Keijser de TH, Mittemeijer EJ. Lattice parameters of iron-carbon and iron-nitrogen martensites and austenites. Scr. Metall. Mater. 1990;24:509–14.
[33] Franceschi M, Yazdanpanah A, Leone D, Pezzato L, Dabalà M. Laser powder bed fusion fabrication of a novel carbide-free bainitic steel: the possibilities and a comparative study with the conventional alloy. Metals 2024;14. https://doi.org/10.3390/met14010113.
[34] Bertolini R, Lizzul L, Pezzato L, Ghiotti A, Bruschi S. Improving surface integrity and corrosion resistance of additive manufactured Ti6Al4V alloy by cryogenic machining. Int J Adv Manuf Technol 2019;104:2839–50. https://doi.org/10.1007/s00170-019-04180-5.
[35] Woo W, An GB, Em VT, De Wald AT, Hill MR. Through-thickness distributions of residual stresses in an 80 Mm thick weld using neutron diffraction and contour method. J Mater Sci 2014;50:784–93. https://doi.org/10.1007/s10853-014-8638-9.
[36] Woo W, An GB, Truman CE, Jiang W, Hill MR. Two-dimensional mapping of residual stresses in a thick dissimilar weld using contour method, deep hole drilling, and neutron diffraction. J Mater Sci 2016;51:10620–31. https://doi.org/10.1007/s10853-016-0283-z.
[37] Woo W, Em V, Mikula P, An GB, Seong BS. Neutron diffraction measurements of residual stresses in a 50mm thick weld. Mater. Sci. Eng. A 2011;528:4120–4. https://doi.org/10.1016/j.msea.2011.02.009.
[38] Jiang J, Zhang J, Liu J, Chiew SP, Lee CK. Effect of welding and heat treatment on strength of high-strength steel columns. J Constr Steel Res 2018;151:238–52. https://doi.org/10.1016/j.jcsr.2018.09.027.
[39] Madhavan S, Kamaraj M, Vijayaraghavan L, Srinivasa Rao K. Microstructure and mechanical properties of aluminium/steel dissimilar weldments: effect of heat input. Mater Sci Technol 2017;33:200–9. https://doi.org/10.1080/02670836.2016.1176716.
[40] Ouali N, Khenfer K, Belkessa B, Fajoui J, Cheniti B, Idir B, Branchu S. Effect of heat input on microstructure, residual stress, and corrosion resistance of UNS 32101 lean duplex stainless steel weld joints. J Mater Eng Perform 2019;28:4252–64. https://doi.org/10.1007/s11665-019-04194-w.
[41] Guo N, Yin XQ, Liang J, Ma N. Effects of heat input on welding buckling distortion by experimental measurement method. Sci Technol Weld Join 2017;22:381–8. https://doi.org/10.1080/13621718.2016.1251079.
[42] Nizam MSH, Marizan S, Zaki SA, Mohd Zamzuri AR. Vision based identification and classification of weld defects in welding environments: a review. Indian J Sci Technol 2016;9:1–15. https://doi.org/10.17485/ijst/2016/v9i20/82779.
[43] Babu SS. The mechanism of acicular ferrite in weld deposits. Curr Opin Solid State Mater Sci 2004;8:267–78. https://doi.org/10.1016/j.cossms.2004.10.001.

[44] Mollaei Milani J, Saeid T. Acicular ferrite nucleation and growth in API5L-X65 steel submerged arc welded joints. Mater Sci Technol 2020;36:1398–406. https://doi.org/10.1080/02670836.2020.1783774.
[45] Morsdorf L, Emelina E, Gault B, Herbig M, Tasan CC. Carbon redistribution in quenched and tempered lath martensite. Acta Mater 2021;205:116521. https://doi.org/10.1016/j.actamat.2020.116521.
[46] García De Andrés C, Caballero FG, Capdevila C, Álvarez LF. Application of dilatometric analysis to the study of solid-solid phase transformations in steels. Mater Char 2002;48:101–11. https://doi.org/10.1016/S1044-5803(02)00259-0.
[47] Bhadeshia HKDH. Bainite in steels: theory and practice, vol 19. Maney Publishing; 2006. ISBN 9781909662742.
[48] Sourmail T, Smanio V. Determination of ms temperature: methods, meaning and influence of "slow start" phenomenon. Mater Sci Technol 2013;29:883–8. https://doi.org/10.1179/1743284713Y.0000000209.
[49] Kawata H, Hayashi K, Sugiura N, Yoshinaga N, Takahashi M. Effect of martensite in initial structure on bainite transformation. Mater Sci Forum 2010;638–642:3307–12. https://dx.doi.org/10.4028/www.scientific.net/MSF.638-642.3307.
[50] Toji Y, Matsuda H, Raabe D. Effect of Si on the acceleration of bainite transformation by pre-existing martensite. Acta Mater 2016;116:250–62. https://doi.org/10.1016/j.actamat.2016.06.044.
[51] Garcia-Mateo C, Jimenez JA, Lopez-Ezquerra B, Rementeria R, Morales-Rivas L, Kuntz M, Caballero FG. Analyzing the scale of the bainitic ferrite plates by XRD, SEM and TEM. Mater Char 2016;122:83–9. https://doi.org/10.1016/j.matchar.2016.10.023.